





Cite this: *New J. Chem.*, 2021, 45, 6940

Hemin-based conjugated effect synthesis of Fe–N/CNT catalysts for enhanced oxygen reduction†

Yue Lu,^a Han Zhang,^b *^a Shaojun Liu,^a Chenglong Li,^a Lixiang Li,^a Baigang An ^a and Chengguo Sun*^{ab}

Metal–nitrogen codoped cathode catalysts, such as M–N–C (M = Fe, Co, Mn, etc.) are considered most promising non-platinum group ORR catalysts, and have received widespread attention. However, the problem involving the high oxygen reduction performance and stability of the catalyst remains to be solved. The unique olefin oxidation polymerization and π – π stacking effect induced hemin to be evenly coated on polypyrrole nanotubes (PPy). Subsequent carbonization produces the Fe–NCNT catalyst with a monodispersed, uniform diameter and large inner cavity. The PPy not only serves as a template for the formation of the hemin polymer, but also provides C, N source to further improve the catalytic activity. The material exhibits excellent ORR activity attributed to the promotion of the π – π stacking effect between hemin and PPy, and the abundant active site of Fe–N_x derived from hemin. Results show that the Fe–NCNT-800 catalyst with high performance exhibits a maximum onset potential ($E_{\text{onset}} = 0.93$ V) and half-wave potential ($E_{1/2} = 0.79$ V). The RRDE measures points out the complete four-electron transfer pathway of the Fe–NCNT-800 catalyst. The Fe–NCNT catalysts have higher durability of a negligible negative shift (10 mV) of $E_{1/2}$ after a 5000 cycle ADT, and a remarkable methanol tolerance capability that is superior to that of the Pt/C catalyst. The synergy between the PPy-derived N-doped carbon nanotubes and Fe–N_x facilitates oxygen reduction and electron conduction.

Received 3rd January 2021,
 Accepted 19th March 2021

DOI: 10.1039/d1nj00020a

rsc.li/njc

1. Introduction

The growing energy demand, depletion of fossil fuels, and worsening environmental pollution have motivated vast technologies, such as proton exchange membrane fuel cells (PEMFCs), which are the most popular electrochemical energy storage and conversion devices.^{1,2} They can convert chemical energy into electrical, reacting with hydrogen to form water. Precious metal-based catalysts, such as Pt-based catalysts, are highly effective ORR cathodic catalysts. However, the limiting of their high cost, poor stability, susceptibility to CO poisoning, and poor methanol resistance, hampers large-scale production applications.^{3–7} Therefore, it is important to develop high-performance, stable and wide-ranging electrocatalysts to replace precious metal catalysts.⁸

Carbon materials occupy an important position in energy storage and conversion materials (e.g., fuel cells and lithium ion batteries) due to their ultra-high stability, excellent electrical conductivity, modifiable structure, and functionality.^{9,10} Some examples include carbon nanotubes,^{11,12} carbon fibers,^{13,14}

few-layer graphene,¹⁵ spherical activated carbon,¹⁶ and carbon black,¹⁷ which are repeatedly applied as templates to support precursor materials. In particular, carbon nanotubes and few-layer graphene are called suitable carrier candidates with excellent performance due to their light weight properties and high conductivity.^{18,19} Generally, heteroatom-doped carbon materials with their excellent catalytic performance activity, low cost, and perfect chemical stability have demonstrated enormous potential for improving the ORR reactivity.²⁰ Since the radius of N atoms is smaller than that of C atoms, the electron-withdrawing properties of N atoms will produce a net positive charge on adjacent carbon atoms, which is conducive to the adsorption of O₂ and promotes the breaking of the O=O bond, thereby increasing the oxygen reduction capacity of N-doped carbon materials.⁷ Hetero-atom-doped carbon-based ORR catalysts can be divided into metal-free heteroatom (N, B, P and S)-doped carbon-based catalysts^{7,21–23} and non-noble metal (Fe, Co, Mn and Ni)-doped catalysts.²⁴ Recently, iron–nitrogen–carbon elements (Fe–N–C) catalyst materials were considered most promising alternatives to Pt-based catalysts with high cost and scarcity for ORR with comparable performance to Pt-based catalysts.^{25,26} However, it is difficult to determine the true reaction center of most well-developed Fe–N–C catalysts, and the interpretation of the main reason for the high activity for ORR is still in debate.^{27,28} Comparing the XPS and infrared spectra of N-doped materials before and after

^a School of Chemical Engineering, University of Science and Technology Liaoning, Anshan 114051, China. E-mail: cgsun@njjust.edu.cn, hzhang0807@163.com

^b School of Chemical Engineering, Nanjing University of Science and Technology, Xiaolingwei 200, Nanjing, Jiangsu 210094, China

† Electronic supplementary information (ESI) available. See DOI: 10.1039/d1nj00020a

ORR under alkaline conditions, it is speculated that the ortho carbon atom of pyridinic nitrogen is attached to a hydroxyl group during the ORR reaction, which is an intermediate of the oxidative reaction. Pyridine nitrogen plays an important role in the oxygen reduction reaction, while the ortho carbon next to the pyridinium nitrogen is the active site of oxygen reduction.²⁹ Hossen *et al.* proved that the presence of a higher amount of surface oxides and pyridinic N is the main reason for the better performance towards ORR in alkaline media with different Fe–N–C oxygen reduction reaction catalysts.³⁰

How to be promising candidates for the ORR electrocatalyst often requires two factors to consider: first, the maximized active site with an exposed active site in the active substance; second, the pores and surface structure of the template material to anchor and expose the active sites.^{31,32} The porphyrin-based biomass material due to its highly conjugated structure (M–N₄), and cheap advantage is regarded as the most popular precursor.³³

Herein, we have developed a facile olefin oxidation polymerization approach to synthesize hollow tubular Fe/N-codoped carbon nanotubes (Fe–NCNT) for ORR catalysts. The formation of this structure originates from the π – π stacking effect between the precursor of polypyrrole nanotubes and hemin, which is different from physical adsorption. The remarkable electrocatalytic performance and stability was attributed to the uniform decoration of Fe–N_x active sites on the surface of the carbon nanotubes, and was beneficial to rapid mass transfer. The ORR performance was achieved with the half-wave potential ($E_{1/2}$) of 0.79 V, and exhibited first-rate performance methanol resistance and higher stability in 0.1 M KOH. A catalytic performance comparable to Pt has been demonstrated, making it a good candidate for ORR electrocatalysts in energy storage/conversion and other related applications.

2. Experimental

2.1 Materials and instrument

All chemicals were directly used without purification. Hemin was purchased from the Hetianlong Biotechnology Co., Ltd. The standard catalyst of Pt/C (20% Pt on Vulcan XC-72) was purchased from Johnson Matthey Company, and 5 wt% Nafion solution was purchased from DuPont Co., Ltd. N-Doped carbon nanotubes were purchased from Pioneer Nanomaterials Technology. Other chemicals and all solvents were received from Sinopharm Chemical Reagent Company. The horizontal tubular resistance furnace (model: EXPRESS-LINE) was purchased from Thermcraft Electric Furnace Co., Ltd of the United States.

The morphologies, composition, and structure of the products were characterized by SEM (Apreos), TEM (Tecnai G2 F20), XRD (D/Max2500 with Cu K α radiation), FT-IR (EQUINOX55), BET method N₂ adsorption isotherm (ASAP-2020), Raman (HORIBA Xplora Plus) and XPS (PHI5300X).

2.2 Synthesis of PPy

The polypyrrole nanotubes (PPy) were prepared using the soft template method with modified procedures.^{34,35} Methyl orange (49 mg, 0.15 mmol) as a surfactant was dissolved in 20 mL deionized water, and the pyrrole monomer (105 μ L, 1.5 mmol)

was poured into the solution. 10 mL of deionized water containing FeCl₃·6H₂O (405 mg, 1.5 mmol) was added dropwise to the above solution, and kept for 24 h at room temperature under stirring. After the reaction, the filter was washed and filtered with a large amount of deionized water and ethanol for several times. The product was dried in a 40 °C vacuum oven and denoted as PPy.

2.3 Activation of PPy and synthesis of hemin–PPy, hemin–NCNT

A certain amount of PPy nanotubes were mounted into a muffle furnace, heated to 300 °C and maintained for 1 h. The furnace was then allowed to cool naturally to room temperature (RT), and the activated product was denoted as activation-PPy (A-PPy nanotubes).

A-PPy (30 mg) and hemin (30 mg) were dispersed in 40 mL *N,N*-dimethylformamide (DMF, 40 mL) under sonication, and heated to 80 °C in the oil bath. Then, azobisisobutyronitrile (AIBN) initiator was added in the mixture solution, and the reaction was kept at 80 °C for 24 h under stirring. After cooling to RT, the product was washed several times with ethanol and deionized water, and dried under vacuum at 60 °C for 6 h. The as-prepared black solid was denoted as hemin–PPy.

Under the same conditions, a comparative sample was prepared using N-doped carbon nanotubes purchased from Xianfeng Nanomaterials Technology Co., Ltd as a template, which was labeled hemin–NCNT.

2.4 Synthesis of Fe–NCNT, NCNT, C–Fe–NCNT

The hemin–PPy was placed in a horizontal tube furnace, and was heated for 2 h at 5 °C min^{−1} under Ar atmosphere and maintained for different temperatures (700, 800, 900 and 1000 °C). The furnace was then allowed to cool naturally to RT, and the final product was denoted as Fe–NCNT-*X* (*X* = 700–1000). According to different mass ratios of A-PPy and hemin, the obtained powders were named as Fe–NCNT (5:30, 15:30, 50:30). N-Doped carbon nanotubes (NCNT) and C–Fe–NCNT were prepared with the form A-PPy and hemin–NCNT under the same procedure for Fe–NCNT.

2.5 Electrochemical characterization

Electrochemical measurements were accomplished in a three-electrode system using a Garmy Reference 3000 potentiostat (Garmy Instruments, USA). Ag/AgCl was used as a reference electrode, and a square platinum plate having a side length of 1 cm was used as the counter electrode. The operation experiments were all performed at room temperature. The glassy carbon electrode was polished on the suede material with a 0.5 μ m polishing powder (Al₂O₃) suspension before the ink was dispensed. All potentials were converted to the potential *versus* RHE according to $E_{(RHE)} = E_{(Ag/AgCl)} + 0.0592 \times \text{pH} + 0.1989$ when measured against an Ag/AgCl electrode in this study.

As to the working electrode preparation, 4 mg of the sample was dispersed ultrasonically in a mixture of ethanol (400 μ L), isopropanol (100 μ L) and Nafion (25 μ L, 5 wt%) to form a uniform suspension. The catalyst ink (8 μ L) was pipetted onto the polished glassy carbon electrode with a diameter of 5 mm for all samples, including commercial Pt/C.

The electrochemical test conditions of the catalyst sample are as follows: the cyclic voltammetry (CV) was cycled 5 times in N_2 and O_2 -saturated 0.1 M KOH solution at potential between 1.169 V to 0.169 V at a scan rate of 50 mV s^{-1} . Linear sweep voltammetry (LSV) was measured in O_2 -saturated 0.1 M KOH solution at different rotating rates from 400 to 2500 rpm with a scan rate of 10 mV s^{-1} . The methanol tolerance test and the durability test of the catalyst were all measured by a constant voltage current method. The methanol tolerance test was taken before and after adding 5 M methanol in O_2 -saturated 0.1 M KOH solution. The experimental setup parameters and conditions of the durability test of the catalyst were identical, except that the time was set to 8 h. The stability test was measured at 1600 rpm in O_2 -saturated 0.1 M KOH solution before and after 5000 cycles of LSV testing at a scan rate of 10 mV s^{-1} .

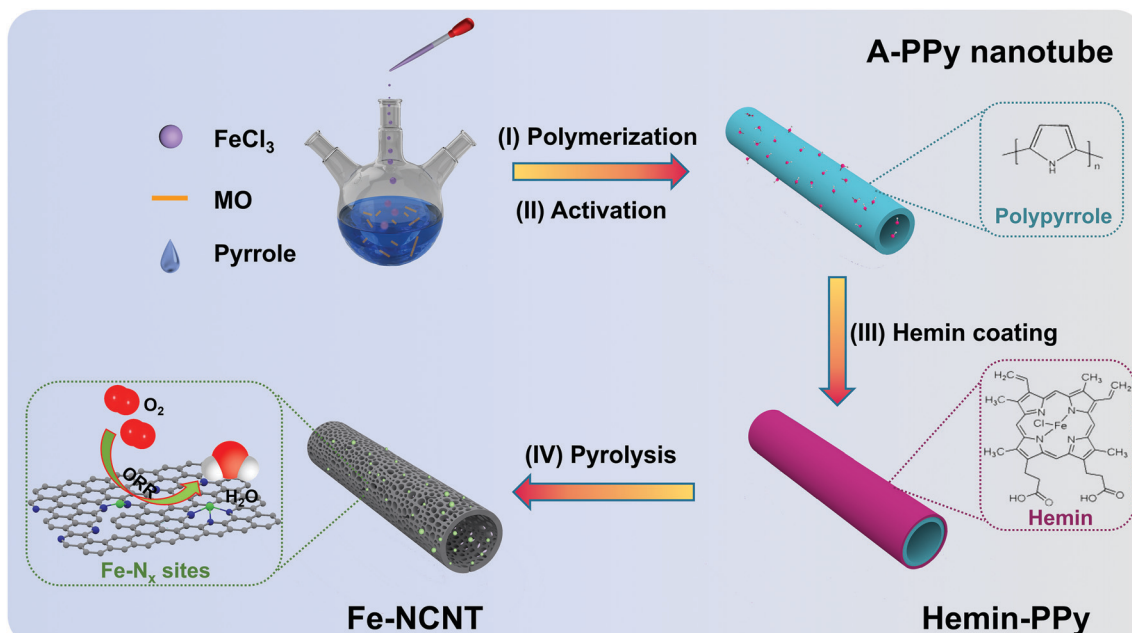
The electron transfer number (n) and the kinetic limit current density (J_k) were calculated by the K-L equation, which is the relationship between the reciprocal of the experimentally measured current density (J^{-1}) and the number of revolutions ($\omega^{-1/2}$). The relationship is a straight line, which can be used to calculate the number of transferred electrons by the slope. The reciprocal of the intercept is the dynamic limit current density J_k .

In the RRDE test, the disk electrode was scanned cathodically in an O_2 -saturated 0.1 M KOH solution. The ring potential was maintained at 1.25 V (V vs. RHE), and the scan rate was 0.5 mV s^{-1} . The electron transfer number (n) and the HO_2^- yield can be calculated according to the equation.³⁶

3. Results and discussion

The synthesis strategy of Fe-NCNT- X ($X = 700\text{--}1000$) is schematically illustrated in Scheme 1. First, polypyrrole (PPy) with a hollow tubular structure was prepared by using the soft

template method with methyl orange (MO) as the soft template. The morphological structure of the as-prepared products was investigated through scanning electron microscope (SEM) and transmission electron microscopy (TEM). Fig. 1a and b show that PPy has the diameter of about 200 nm and a wall thickness of about 30 nm. The lengths of the nanotubes are up to several micrometers. It demonstrates that the monodispersed, uniform diameter and smooth surface hollow tube structures have been successfully prepared (Fig. S2, ESI[†]). Second, the PPy was activated at 300°C in the air to improve the dispersibility of PPy in DMF (noted as A-PPy). As shown in Fig. 1c, the PPy and A-PPy nanotubes can disperse in DMF well, and form black mixtures after sonicating at room temperature. However, after standing for 1 day at room temperature, PPy slowly settled down and the DMF became clear. In contrast, A-PPy still remained as a good dispersion. The long-term dispersion and stability of A-PPy can be attributed to the oxygen-containing groups ($-O-C$, $C=O$) and defect of A-PPy containing the higher solubility onto the surface of PPy. Then, AIBN-initiator induced hemin to be polymerized on the outer wall of A-PPy in the manner of olefin polymerization like a coating using the strong π - π stacking effect (hemin-PPy, Fig. S1, ESI[†]), which effectively restrained the hemin to have uneven stacking and enhanced conductivity.³⁷ SEM and TEM images of A-PPy is shown in Fig. S3 (ESI[†]). PPy-300 still maintained a hollow tubular structure after 1 h at 300°C in air. Finally, Fe/N-codoped carbon nanotubes (Fe-NCNT) were obtained by annealing the intermediates at different temperatures ($700\text{--}1000^\circ\text{C}$) in an Ar atmosphere. The SEM images of the as-obtained Fe-NCNT were not only free from agglomeration, but also uniform in diameter. As shown in Fig. 1e and f, the surfaces of the nanotubes become rough and porous after treatment under flowing Ar. Meanwhile, the average thickness of the nanotube wall



Scheme 1 Schematic illustration of the Fe/N-codoped carbon nanotubes electrocatalyst.

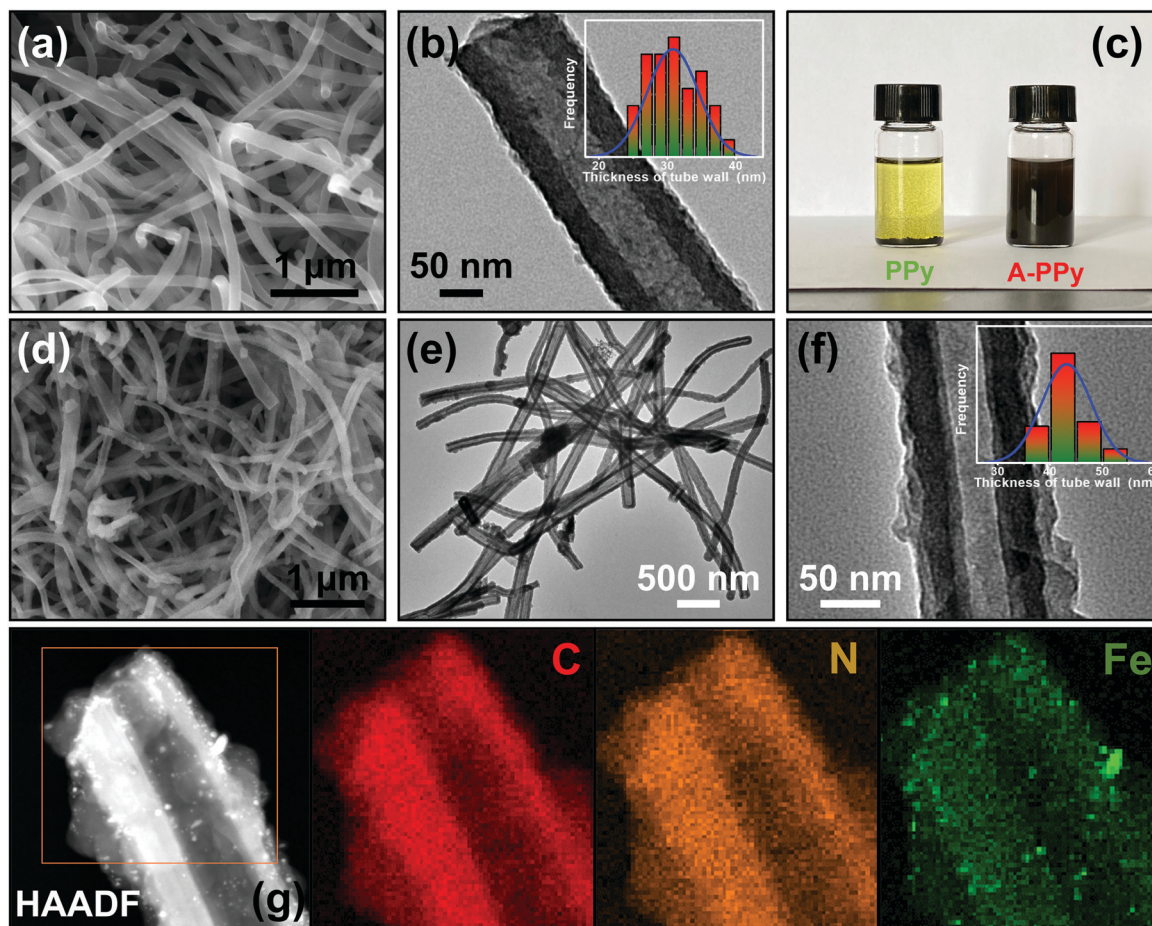


Fig. 1 SEM images of (a) PPy and (d) Fe-NCNT-800. TEM images of (b) PPy, and (e and f) Fe-NCNT-800 (the inset is the thickness of the nanotube wall distribution histogram). (c) Digital photograph of the equivalent PPy and A-PPy nanotubes dispersed in DMF (4 mL) at room temperature for 1 day. (g) HAADF-STEM image of Fe-NCNT-800 and corresponding elemental maps of C, N and Fe.

changed from 30 nm (original PPy) to about 43 nm (inset of Fig. 1b and f). Moreover, the formation of carbon nanotubes throughout the PPy-derived catalysts may enhance the electronic conductivity and corrosion resistance of the catalyst.³³ The high-angle annular dark field-scanning transmission electron microscope (HAADF-STEM) images and corresponding energy-dispersive X-ray (EDX) mapping analysis of Fe-NCNT-800 (Fig. 1g and Fig. S4, ESI[†]) reveal that C, N and Fe are homogeneously distributed along the catalyst, which could also be observed from the results obtained by the full spectrum of XPS (Fig. S7, ESI[†]). In contrast, the direct calcination of PPy at 800 °C under Ar atmosphere without hemin coating resulted in the formation of the N-doped carbon nanotubes (noted as NCNT, Fig. S12, ESI[†]).

The FT-IR spectra of PPy, A-PPy, hemin-PPy and Fe-NCNT are shown in Fig. 2a. The infrared characteristic peak of PPy is 1539 cm^{-1} , which corresponds to the C-C stretching vibration on the pyrrole ring. The C-N stretching vibration occurs at 1475 and 1445 cm^{-1} , and the 1162 cm^{-1} peak is the plane deformation vibration of C-H and C-N. The 900 and 778 cm^{-1} features correspond to the C-H deformation vibration outside the plane of the ring. The presence of PPy was confirmed by the

characteristic peaks and SEM (Fig. 1a). The spectra of the hemin-PPy exhibited interesting features at 1000 cm^{-1} , which corresponds to the vibration peak of the porphyrin skeleton. In the 1700 cm^{-1} region, the spectrum of hemin-PPy is dominated by the signals of the C=O characteristic peak of -COOH in hemin, which proved that hemin succeeded in a functionalized modification on A-PPy. After pyrolysis at high temperature, Fig. S5 (ESI[†]) illustrated that the infrared characteristic absorption peaks of the pyrrole and porphyrin rings in Fe-NCNT ($X = 700\text{--}1000$) disappear, which suggests the transformation of the pyrrole and porphyrin rings into Fe/N-codoped carbon nanotubes.^{34,35}

X-Ray diffraction (XRD) was performed to investigate the crystallographic phase of the as-prepared composites. The diffraction peak at around 25.0° and 44.5° corresponds to the (002) and (101) planes of the graphite structure (Fig. 2b). The XRD peaks of Fe-NCNT-700 and Fe-NCNT-800 indicate the presence of Fe₂O₃ (JCPDS No. 01-1053) and Fe₃O₄ (JCPDS No. 75-0033). The experimental parameters were carefully explored *via* control experiments. With the increasing pyrolysis temperature, Fe (JCPDS No. 87-0721) and Fe₃C (JCPDS No. 85-1317) were observed, resulting from the reaction of the Fe species with graphite carbon derived from PPy and hemin.

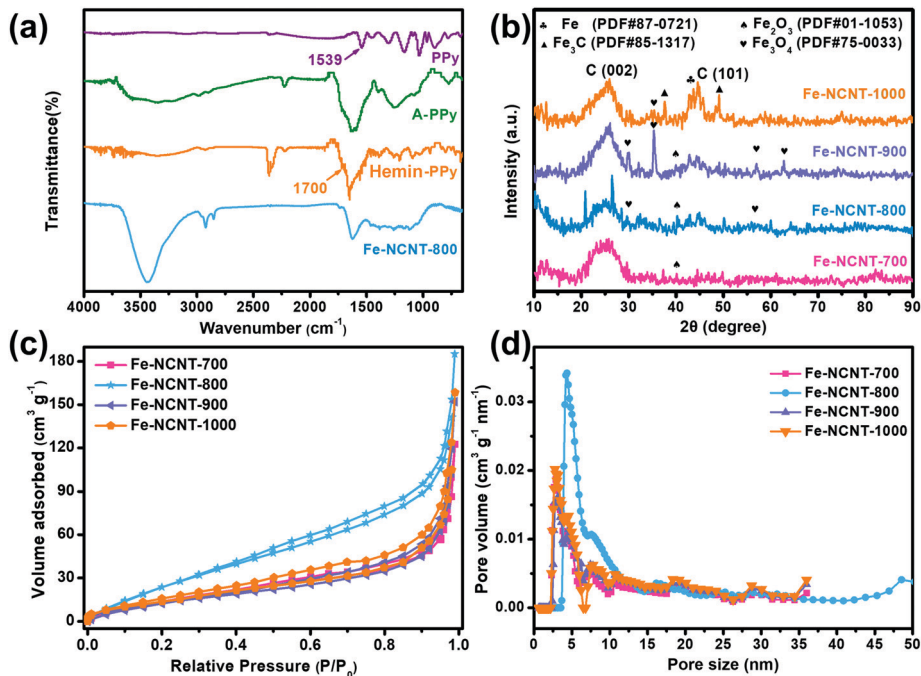


Fig. 2 The FT-IR spectrum of (a) PPy, A-PPy, hemin-PPy and Fe-NCNT-800. (b) XRD patterns of the Fe-NCNT-*X* (*X* = 700–1000) catalyst. (c and d) N₂ adsorption-desorption isotherm and the corresponding pore size distribution of Fe-NCNT-*X* (*X* = 700–1000).

The N₂ adsorption-desorption isotherms of Fe-NCNT-*X* (*X* = 700–1000) are type IV profiles (Fig. 2c and Table S1, ESI[†]), indicating the presence of mesopores and micropores in these samples. The surface areas of Fe-NCNT-700, 800, 900 and 1000 are 52.5, 104.3, 48.7 and 55.2 m² g⁻¹, respectively. The pore size distribution calculated by the DFT method, as shown in Fig. 2d, indicates that the samples are mainly controlled by the mesoporous structure, and the total pore volumes of Fe-NCNT-*X* (*X* = 700–1000) are 0.19, 0.29, 0.24 and 0.25 cm³ g⁻¹ (Fig. 2d). The Barrett-Joyner-Halenda (BJH) pore size distribution showed that the four samples have large pore structures of between 56–57 nm, which is the central pore size of the nanotube structure (Fig. S6, ESI[†]). The change in the specific surface area depends on the temperature of the pyrolysis. The pyrolysis temperature was increased from 700 °C to 800 °C, and the specific surface area was doubled. However, at a higher temperature up to 900 °C, the specific surface area rapidly decreases. Excessive temperature causes the collapse of the structural pores. Therefore, the specific surface area of the Fe-NCNT-800 reaches the maximum and the most pores, it facilitates the adsorption of O₂ and electron transport, and promotes the progress of the ORR reaction.^{38,39}

X-Ray photoelectron spectroscopy (XPS) was used to determine the chemical composition, chemical state, and bond type between the elements of the Fe-NCNT-*X* (700–1000) catalyst. As expected, the presence of C, N and Fe elements in the four catalyst samples is shown in the survey spectra of the XPS measurements (Fig. S7, ESI[†]). In addition, the high-resolution N 1s spectrum of the samples under different pyrolysis temperatures can be deconvoluted into five peaks: pyridinic N (398.4 eV), Fe-N_{*x*} (399.2 eV), pyrrole N (400.8 eV), graphite N

(402.4 eV) and oxidized N (404.2 eV) (Fig. 3 and Fig. S8, ESI[†]),^{40,41} and the relative content of the N sites is summarized in Table S2 (ESI[†]). The relative content of graphitic N and graphite oxidized N content increased with the increase in temperature from 800 °C to 1000 °C. Interestingly, the Fe-NCNT-800 sample has the relative largest content of pyridinic-N and Fe-N_{*x*} content. According to the previous reports, it has been demonstrated that Fe-N_{*x*} is mainly responsible for the electrocatalytic activity in ORR.⁴² The Fe species was anchored in the Fe/N-codoped carbon nanotubes by olefin polymerization and pyrolysis process, and the dominant Fe-N coordination bonds were postulated to be planar Fe-N₄ and Fe-N₂, respectively (Scheme 1). Moreover, the pyridinic N can generate Lewis base sites, and the carbon atom next to pyridinic N is favorable for O₂ adsorption during the ORR reaction, having a good electron transfer rate and promoting the cleavage of O-O under alkaline conditions.³⁰ Therefore, the high Fe-N_{*x*} and pyridinic N content is an important reason for Fe-NCNT-800 excellent oxygen reduction performance.

The Fe element in the Fe-NCNT-800 composite material was contributed by hemin (Fig. 3c and Fig. S16, ESI[†]). The high-resolution spectra of the Fe 2p electrons of the Fe-NCNT-800 composite material were deconvoluted into two pairs of peaks: Fe²⁺ (710.6 eV and 722.3 eV) and Fe³⁺ (712.9 eV and 725.0 eV), and the satellite peak is 717.8 eV^{43,45} (Fig. 3c, Fig. S9 and Table S3, ESI[†]). Only the Fe-NCNT-1000 sample contained the Fe(0) species, implying that the iron species was reduced to form metallic elements or clusters of metallic elements at higher temperature conditions, corresponding to the XRD test results (Fig. 2b). The Fe-NCNT-800 sample was further analyzed by depth XPS with different etching times of Ar plasma treatment.

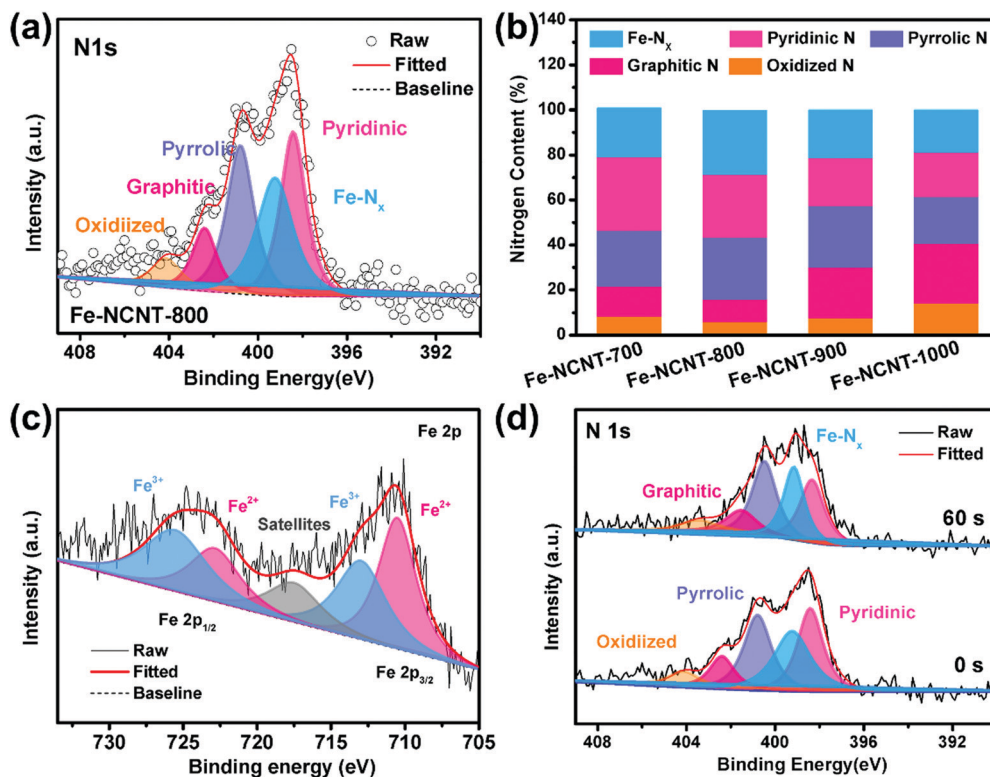


Fig. 3 (a) High-resolution XPS spectroscopy of N 1s of Fe-NCNT-800, (b) nitrogen content in Fe-NCNT-X ($X = 700$ – 1000) of four different N configurations, (c) high-resolution XPS spectroscopy of Fe 2p of Fe-NCNT-800, (d) depth XPS spectra of N 1s for Fe-NCNT-800 at an Ar etching time of 0 and 60 s.

The high-resolution depth spectra of N 1s shows that, compared with the original Fe-NCNT-800, the etching time is 60 s, and the photoelectrons go through the hemin-derived carbon shell. The relative content of graphitic N increased proportionally, while the Fe- N_x and pyridinic-N contents decreased with Ar plasma treatment, proving that hemin succeeded in functionalized modification on the PPy nanotubes (Fig. 3d and Table S5, ESI[†]). The high-resolution XPS of the Fe 2p electrons and the corresponding element atomic content of the Fe-NCNT-800 samples at different etching times are shown in Fig. S17 and Table S7 (ESI[†]). It reveals that the iron content of the Fe-NCNT-800 composite material changes slightly with the increase of the etching time, which confirmed that the Fe element is uniformly distributed throughout the Fe-NCNT-800 composite nanotube. This is consistent with the Fe element mapping in the HAADF-STEM image of the tested Fe-NCNT-800.

The unique structures and compositions mentioned above were used to explore the catalytic activity of the samples toward ORR, which were performed by rotating disk electrode (RDE) at room temperature. The cycle voltammetry (CV) was carried out in 0.1 M KOH solution with O_2 -saturated or N_2 -saturated conditions (Fig. 4a). A well-defined oxygen reduction peak was observed at 0.77 V (V vs. RHE), which indicates that Fe-NCNT-800 can undergo oxygen reduction reaction under O_2 saturation. However, no reaction peak emerged in the N_2 -saturation solution in the same voltage window. To estimate the electrocatalytic activities, the CV curves of Fe-NCNT

(different pyrolysis temperature and mass ratio of PPy/hemin) were also tested (Fig. 5a and Fig. S10, ESI[†]). Notably, the reduction peak position for Fe-NCNT-800 occurs at 0.77 V, and is higher than those of Fe-NCNT-X ($X = 700, 900$ and 1000), implying the superior catalytic activity of Fe-NCNT-800 among these catalysts.^{44,45}

In order to gain deeper insight into the electrocatalytic activity and kinetics, the linear scanning voltammetry (LSV) curves of Fe-NCNT-800, C-Fe-NCNT-800, NCNT-800 and commercial Pt/C were recorded on RDE with a rotation rate of 1600 rpm at a scan rate of 10 mV s^{-1} (Fig. 4b and Table S6, ESI[†]). When compared with Fe-NCNT and commercially Pt/C catalysts, the best ORR activity was achieved by Fe-NCNT-800, as judged by the maximum onset potential (E_{onset}) of 0.93 V and halfwave potential ($E_{1/2}$) of 0.79 V, which is close to the Pt/C with E_{onset} of 1.06 V and $E_{1/2}$ of 0.82 V. It was worth mentioning that Fe-NCNT-800 had the largest limit current density (-5.02 mA cm^{-2}), exceeding Pt/C (-4.64 mA cm^{-2}). This result can infer that the Fe- N_x active sites have a strong interaction with peroxide, which is beneficial to promote the four-electron reduction process of ORR. In contrast, the NCNT-800 catalyst shows poor catalytic activity, indicating that the N-doped PPy-based catalyst barely contributed much to improving the overall activity of the catalyst. The ORR activity is significantly enhanced as the hemin was coated on PPy, implying that the activity of the Fe-NCNT-800 catalyst can be largely attributed to the Fe- N_x sites instead of the C- N_x sites. In addition,

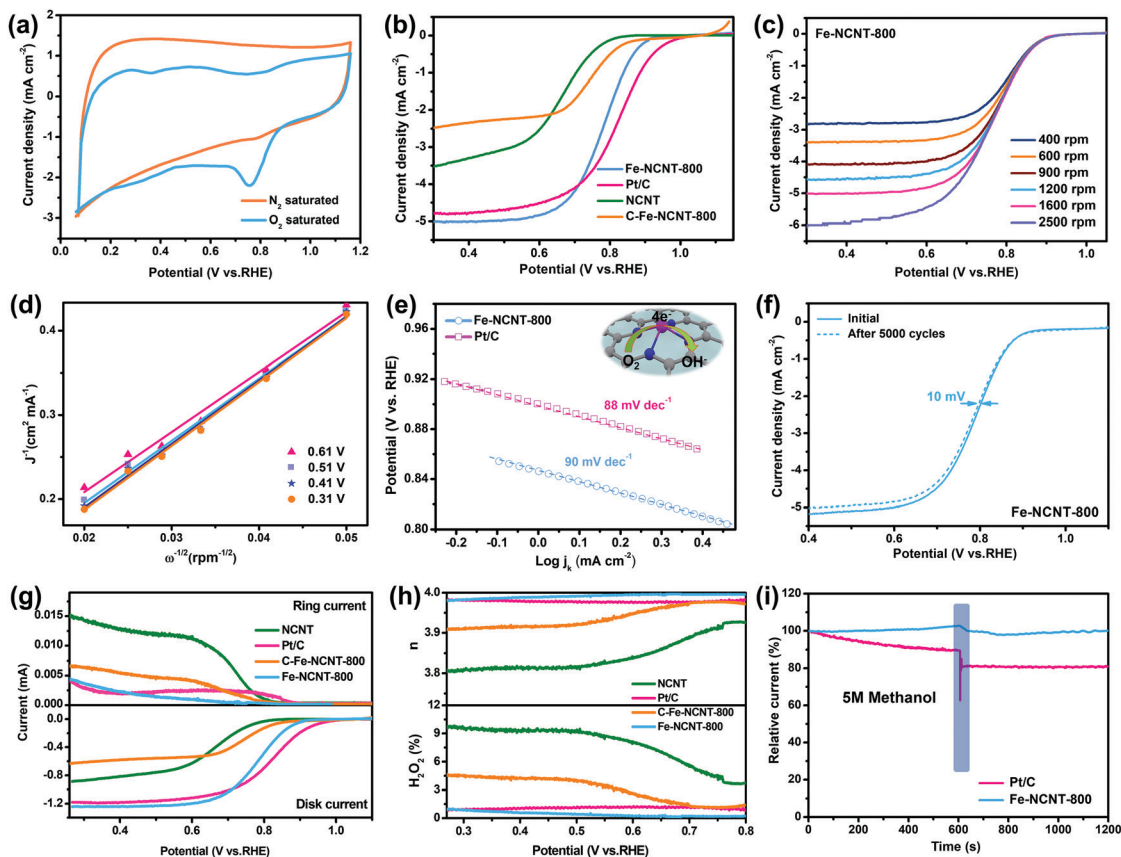


Fig. 4 Electrocatalytic performance evaluation of Fe-NCNT- X ($X = 700-1000$), NCNT and commercial Pt/C in O_2 -saturated 0.1 M KOH solution. (a) CV curves of Fe-NCNT-800 in N_2 -saturated and O_2 -saturated 0.1 M KOH at a scan rate of 50 mV s^{-1} . (b) LSV curves of Fe-NCNT-800, C-Fe-NCNT-800, NCNT and the Pt/C catalyst at 1600 rpm. (c) LSV polarization curves of Fe-NCNT-800 at different rotation rates from 400 to 2500 rpm and inset: the fitted K-L plots of Fe-NCNT-800 at different potentials. (d) The inset figure is the K-L plots of Fe-NCNT-800 ($\omega^{-1/2}$ vs. $j^{-1/2}$), ω and j are the speed of the angular rotation and current density, respectively). (e) Tafel slopes of Fe-NCNT-800 and Pt/C. (f) LSV before and after a 5000 cycle ADT of ORR on Fe-NCNT-800 in O_2 -saturated 0.1 M KOH. (g) RRDE measurements for Fe-NCNT-800, C-Fe-NCNT-800, NCNT and the Pt/C catalyst. (h) H_2O_2 yield and electron transfer number (n) of Fe-NCNT-800, C-Fe-NCNT-800, NCNT-800 and Pt/C. (i) Chronoamperometric responses of Pt/C and Fe-NCNT-800 catalysts with sequential injection of O_2 -saturated 5 M MeOH at 600 s.

comparing the performance of the C-Fe-NCNT-800 samples prepared from commercial N-doped carbon tubes (Fig. 4b and Fig. S13, ESI †), it further highlights the excellent performance of the Fe-NCNT-800 sample, which is attributed to the fact that the activated A-PPy is more conducive to the π - π uniform modification of hemin, making the active sites of the derived Fe-NCNT more uniform. It is noteworthy that our Fe-NCNT is superior to most carbon Fe-N-C electrocatalysts previously reported (Table S8, ESI †).

Furthermore, the electron transferred number (n) and kinetic current density (J_k) of Fe-NCNT- X ($X = 700-1000$) were determined according to the LSV curves calculated from the Koutecky-Levich (K-L) equation. The good parallel linearity of the K-L plots of Fe-NCNT-800 from 0.3 to 0.6 V indicated first-order reaction kinetics for ORR (Fig. 4d). Notably, the Fe-NCNT-800 exhibited highly kinetic current density J_k of 28.23 mA cm^{-2} and a 4-electron ORR reaction mechanism close to Pt/C, as shown in Fig. S15 (ESI †).^{3,46-48} According to the LSV curves, the calculated Tafel slope of the Fe-NCNT-800 catalyst (90 mV dec^{-1}) was smaller than that for Pt/C (88 mV dec^{-1}),

suggesting the superior ORR kinetics of Fe-NCNT-800 and the advantage of hollow nanotube structures for the electrocatalytic activity (Fig. 4e). In contrast, the effect of the pyrolysis temperature on the ORR performance of the hemin-PPy samples is shown in Fig. 5c and Fig. S15 (ESI †). Fe-NCNT-800 gives the maximum electron transfer number, a number close to that for the 4-electron reaction process of Pt/C. In contrast, the other catalysts obtained under different temperatures at 0.51 V, 700 °C and 900 °C exhibited lower electron transfer numbers close to that of the 3-electron reaction process, indicating the poorer selectivity in the ORR electrocatalytic system. It should be noted that the electron transfer number of Fe-NCNT-1000 has not yet reached the 3-electron reaction process, suggesting that the atomically dispersed Fe sites aggregated into metallic Fe particles or clusters in the excessive temperature can reduce the electrocatalytic behavior during the reduction process.

To further evaluate the ORR pathway of the catalyst in this study and determine the amount of H_2O_2 produced, a rotating ring disk electrode (RRDE) measurement was performed. In fact, the production of H_2O_2 will not only reduce the electron

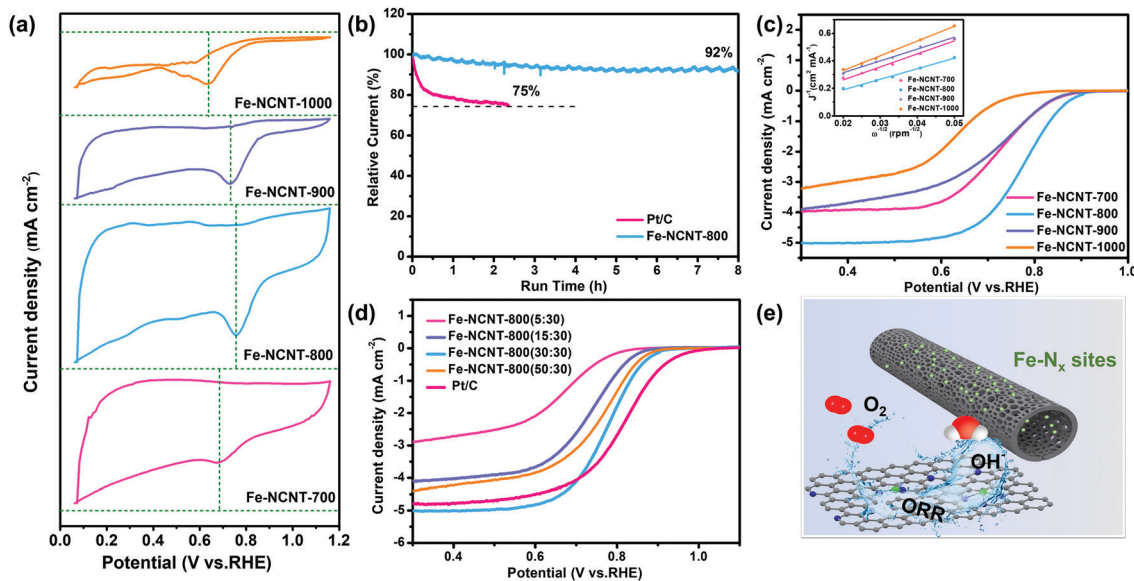


Fig. 5 (a) Cyclic voltammetry (CV) curves of Fe-NCNT- X ($X = 700-1000$) in O_2 -saturated 0.1 M KOH at a scan rate of 50 mV s^{-1} . (b) Chronoamperometric testing of Fe-NCNT-800 and Pt/C in O_2 -saturated 0.1 M KOH. (c) LSV curves of Fe-NCNT- X ($X = 700-1000$) at 1600 rpm and inset: the fitted K-L plots of Fe-NCNT- X ($X = 700-1000$) at 0.51 V. (d) LSV curves of hemin: PPy are synthesized at different ratios (mass ratio) and pyrolyzed at 800°C in O_2 -saturated 0.1 M KOH. (e) Fe/N-doped carbon nanotubes show the potential applications for ORR.

transfer efficiency, but also generate HO_2^- radicals by cracking, which is toxic to electrode materials, such as proton exchange membranes.³⁰ As shown in Fig. 4g, the Fe-NCNT-800 catalyst has the largest disk current of -1.242 mA and a relatively smaller ring current of 0.0041 mA . The H_2O_2 yield percentage is 0.99% and the electron transfer number (n) is also about 4.0 by calculation (Fig. 4h), which indicates that lower H_2O_2 production demonstrates the effective ORR catalytic performance of the Fe-NCNT-800 catalyst and is accompanied by a complete four-electron transfer pathway.

We also compared the durability and methanol sustainability of Fe-NCNT-800 with a standard Pt/C catalyst by chronoamperometry measurement. The current-time ($i-t$) curve for Fe-NCNT-800 delivers almost no current loss after an 8 h length durability test, demonstrating higher stability than the commercial Pt/C (current loss with only 75% current retention just after 2.5 h) (Fig. 5b). The accelerated durability test (ADT) in O_2 -saturated electrolytes was carried out to test the stability of Fe-NCNT-800 and Pt/C for 5000 cycles. The Fe-NCNT-800 exhibited outstanding durability (Fig. 4f), with a negligible negative shift (10 mV) of $E_{1/2}$ after a 5000 cycle ADT, which is superior to Pt/C with a 20 mV shift of $E_{1/2}$ (Fig. S14, ESI[†]). The unexpected stability can be attributed to the covalent binding of Fe- N_x on the outer wall of PPy with good mechanical strength, and the π - π stacking effect between hemin and PPy. As shown in Fig. 4i, a very slight fluctuation in the current density could be observed in Fe-NCNT-800 after the addition of 5 M methanol. However, the Pt/C catalyst shows an enormous current loss due to the methanol oxidation of Pt, indicating that Fe-NCNT-800 had excellent tolerance of methanol crossover effects for ORR. The influence of the synthesized mass ratio of the precursor hemin to PPy nanotubes for ORR activity was investigated in

Fig. 5d and Table S5 (ESI[†]). Obviously, the order of the catalytic activity increase in the alkaline electrolyte is as follows: Fe-NCNT-800 (5:30) < Fe-NCNT-800 (15:30) < Fe-NCNT-800 (50:30) < Fe-NCNT-800 (30:30). With the increase of the precursor hemin content from 5 mg to 30 mg, the catalytic activity of the Fe-NCNT-800 material also gradually increased. This could be attributed to the increase in the number of active centers (Fe- N_x in the catalyst to further enhance the catalytic activity of the Fe-NCNT-800 material. When the amount of hemin that was added increased to 50 mg, the performance of Fe-NCNT-800 (50:30) was reduced. It is explained that the introduction of excessive Fe content will cause the agglomeration of metallic Fe during the pyrolysis process and reduce the electrochemical performance of the catalyst.⁴⁹

4. Conclusions

In summary, we demonstrated an effective approach for the preparation of Fe/N-codoped carbon nanotubes derived from PPy nanotubes as a new efficient ORR catalyst. The olefin oxidation polymerization and π - π stacking effect induced hemin assembly on the template, fabricating the structure of carbon nanotubes decorated with Fe- N_x . The PPy not only serves as a template for the formation of the hemin polymer, but also provides a C, N source to further improve the catalytic activity. The as-prepared Fe-NCNT-800 shows excellent electrocatalytic performance in the reactions of the oxygen reduction. This is attributed to the unique Fe/N-codoped compositions in the carbon skeleton by the π - π stacking effect between hemin and PPy, as well as the superiority of the tubular structure, which affords a high surface area, enhances the utilization

efficiency of the catalytic active sites, shortens the ion diffusion length, and facilitates the charge transfer. This proposed strategy can enlighten the construction of Fe/N-codoped tubular structure, and broaden the application scope of hemin in the fields of energy conversion reactions.

Conflicts of interest

There are no conflicts to declare.

Acknowledgements

The authors gratefully acknowledge the financial support provided by the National Natural Science Foundation of China (21701077, 11972178, 51872131 and 51972156), the Talent Project of Revitalizing Liaoning (XLYC1807114, 2019LNZD01, 2020LNQN17, 2019QN07) and Technology Liaoning Talent Project Grants (601010326).

Notes and references

- P. Zuo, Y. Li, A. Wang, R. Tan, Y. Liu, X. Liang, F. Sheng, G. Tang, L. Ge, L. Wu, Q. Song, N. B. McKeown, Z. Yang and T. Xu, *Angew. Chem., Int. Ed.*, 2020, **6**, 9651–9660.
- L. Gao, M. Xiao, Z. Jin, C. Liu, J. Zhu, J. Ge and W. Xing, *J. Energy Chem.*, 2018, **27**, 1668–1673.
- Y.-J. Wang, W. Long, L. Wang, R. Yuan, A. Ignaszak, B. Fang and D. P. Wilkinson, *Energy Environ. Sci.*, 2018, **11**, 258–275.
- A. Serov, K. Artyushkova, E. Niangar, C. Wang, N. Dale, F. Jaouen, M.-T. Sougrati, Q. Jia, S. Mukerjee and P. Atanassov, *Nano Energy*, 2015, **16**, 293–300.
- S. Alayoglu, A. U. Nilekar, M. Mavrikakis and B. Eichhorn, *Nat. Mater.*, 2008, **7**, 333–338.
- G. Yang, C. Erbay, S.-I. Yi, P. de Figueiredo, R. Sadr, A. Han and C. Yu, *Nano Energy*, 2016, **22**, 607–614.
- C. V. Pham, B. Britton, T. Böhm, S. Holdcroft and S. Thiele, *Adv. Mater. Interfaces*, 2018, **5**, 1800184.
- X. X. Wang, M. T. Swihart and G. Wu, *Nat. Catal.*, 2019, **2**, 578–589.
- W. Wei, D.-w. Wang and Q.-h. Yang, *Carbon*, 2015, **81**, 850.
- S. Cao and J. Yu, *J. Photochem. Photobiol., C*, 2016, **27**, 72–99.
- K. Waki, R. A. Wong, H. S. Oktaviano, T. Fujio, T. Nagai, K. Kimoto and K. Yamada, *Energy Environ. Sci.*, 2014, **7**, 1950–1958.
- R. Du, N. Zhang, J. Zhu, Y. Wang, C. Xu, Y. Hu, N. Mao, H. Xu, W. Duan, L. Zhuang, L. Qu, Y. Hou and J. Zhang, *Small*, 2015, **11**, 3903–3908.
- M. Wu, Y. Wang, Z. Wei, L. Wang, M. Zhuo, J. Zhang, X. Han and J. Ma, *J. Mater. Chem. A*, 2018, **6**, 10918–10925.
- C. Liu, J. Wang, J. Li, J. Liu, C. Wang, X. Sun, J. Shen, W. Han and L. Wang, *J. Mater. Chem. A*, 2017, **5**, 1211–1220.
- C. Lin, L. Yang, L. Ouyang, J. Liu, H. Wang and M. Zhu, *J. Alloys Compd.*, 2017, **728**, 578–584.
- A. J. Romero-Anaya, M. Ouzzine, M. A. Lillo-Ródenas and A. Linares-Solano, *Carbon*, 2014, **68**, 296–307.
- C. Ouyang, B. Ni, Z. Sun, J. Zhuang, H. Xiao and X. Wang, *Chem. Sci.*, 2019, **10**, 2118–2123.
- L. Z. Ouyang, Z. J. Cao, L. L. Li, H. Wang, J. W. Liu, D. Min, Y. W. Chen, F. M. Xiao, R. H. Tang and M. J. I. J. O. H. E. Zhu, *Int. J. Hydrogen Energy*, 2014, **39**, 12765–12772.
- C. Lin, L. Ouyang, C. Zhou, R. Hu and M. J. J. O. P. S. Zhu, *J. Power Sources*, 2019, **443**, 227276.
- J. Gu, S. Magagula, J. Zhao and Z. Chen, *Small Methods*, 2019, **3**, 1800550.
- X. Liu and L. Dai, *Nat. Rev. Mater.*, 2016, **1**, 16064–16076.
- F. Razmjooei, K. P. Singh, D.-S. Yang, W. Cui, Y. H. Jang and J.-S. Yu, *ACS Catal.*, 2017, **7**, 2381–2391.
- C. H. Choi, M. W. Chung, H. C. Kwon, S. H. Park and S. I. Woo, *J. Mater. Chem. A*, 2013, **1**, 3694–3699.
- H. Peng, F. Liu, X. Liu, S. Liao, C. You, X. Tian, H. Nan, F. Luo, H. Song, Z. Fu and P. Huang, *ACS Catal.*, 2014, **4**, 3797–3805.
- H.-Y. Wang, C.-C. Weng and Z.-Y. Yuan, *J. Energy Chem.*, 2021, **56**, 470–485.
- B. Li, S. P. Sasikala, D. H. Kim, J. Bak, I.-D. Kim, E. Cho and S. O. Kim, *Nano Energy*, 2019, **56**, 524–530.
- B.-C. Hu, Z.-Y. Wu, S.-Q. Chu, H.-W. Zhu, H.-W. Liang, J. Zhang and S.-H. Yu, *Energy Environ. Sci.*, 2018, **11**, 2208–2215.
- H. Ren, Y. Wang, Y. Yang, X. Tang, Y. Peng, H. Peng, L. Xiao, J. Lu, H. D. Abruña and L. Zhuang, *ACS Catal.*, 2017, **7**, 6485–6492.
- X. Yang, C. Chen, Z. Zhou and S. Sun, *Acta Phys.-Chim. Sin.*, 2019, **35**, 472–485.
- M. M. Hossen, K. Artyushkova, P. Atanassov and A. Serov, *J. Power Sources*, 2018, **375**, 214–221.
- Y. Han, Y. G. Wang and W. Chen, *J. Am. Chem. Soc.*, 2017, **48**, 17269–17272.
- Z. Ma, L. Xu, L. Liu, L. Wang, X. Zhang and A. Kong, *Dalton Trans.*, 2019, **48**, 2338–2344.
- Z. S. Wu, L. Chen, J. Liu, K. Parvez, H. Liang, J. Shu, H. Sachdev, R. Graf, X. Feng and K. Mullen, *Adv. Mater.*, 2014, **26**, 1450–1455.
- N. V. Blinova, J. Stejskal, M. Trchová, J. Prokeš and M. Omastová, *Eur. Polym. J.*, 2007, **43**, 2331–2341.
- G. Ćirić-Marjanović, S. Mentus, I. Pašti, N. Gavrilov, J. Krstić, J. Travas-Sejdic, L. T. Strover, J. Kopecká, Z. Moravková, M. Trchová and J. Stejskal, *J. Phys. Chem. C*, 2014, **118**, 14770–14784.
- C. C. Yang, S. F. Zai, Y. T. Zhou, L. Du and Q. Jiang, *Adv. Funct. Mater.*, 2019, **29**, 1901949.
- S. Zeng, F. Lyu, L. Sun, Y. Zhan, F.-X. Ma, J. Lu and Y. Y. Li, *Chem. Mater.*, 2019, **31**, 1646–1654.
- Z.-Y. Sui, X. Li, Z.-Y. Sun, H.-C. Tao, P.-Y. Zhang, L. Zhao and B.-H. Han, *Carbon*, 2018, **126**, 111–118.
- C. Si, C. Zhang, J. Sunarso and Z. Zhang, *J. Mater. Chem. A*, 2018, **6**, 19979–19988.
- Y. Chen, H. Wang, S. Ji and R. Wang, *Catal. Commun.*, 2018, **107**, 29–32.
- X. Xu, X. Zhang, Z. Xia, R. Sun, H. Li, J. Wang, S. Yu, S. Wang and G. Sun, *J. Energy Chem.*, 2021, **54**, 579–586.

- 42 J. Woo, S. Y. Yang, Y. J. Sa, W.-Y. Choi, M.-H. Lee, H.-W. Lee, T. J. Shin, T.-Y. Kim and S. H. Joo, *Chem. Mater.*, 2018, **30**, 6684–6701.
- 43 D. H. Lee, W. J. Lee, W. J. Lee, S. O. Kim and Y. H. Kim, *Phys. Rev. Lett.*, 2011, **106**, 175502.
- 44 M. Gong, Z. Deng, D. Xiao, L. Han, T. Zhao, Y. Lu, T. Shen, X. Liu, R. Lin, T. Huang, G. Zhou, H. Xin and D. Wang, *ACS Catal.*, 2019, **9**, 4488–4494.
- 45 W. Niu, L. Li, X. Liu, N. Wang, J. Liu, W. Zhou, Z. Tang and S. Chen, *J. Am. Chem. Soc.*, 2015, **137**, 5555–5562.
- 46 O. T. Holton and J. W. Stevenson, *Platinum Met. Rev.*, 2013, **57**, 259–271.
- 47 X. Peng, T. J. Omasta, E. Magliocca, L. Wang, J. R. Varcoe and W. E. Mustain, *Angew. Chem., Int. Ed.*, 2019, **131**, 1058–1063.
- 48 Q. Liu, X. Liu, L. Zheng and J. Shui, *Angew. Chem., Int. Ed.*, 2018, **130**, 1218–1222.
- 49 Y. Chen, S. Ji, Y. Wang, J. Dong, W. Chen, Z. Li, R. Shen, L. Zheng, Z. Zhuang, D. Wang and Y. Li, *Angew. Chem., Int. Ed.*, 2017, **56**, 6937–6941.